Modelling wind turbine tower-rotor interaction through an aerodynamic damping matrix

Chao Chen Conceptualization; Formal analysis; Methodology; Software; Validation; Writing - Original Draft ,
Philippe Duffour Conceptualization; Supervision; Writing - Review & Editing ,
Paul Fromme Supervision; Methodology; Writing - Review & Editing

PII: S0022-460X(20)30497-1
DOI: https://doi.org/10.1016/j.jsv.2020.115667
Reference: YJSVI 115667

To appear in: *Journal of Sound and Vibration*

Received date: 16 September 2019
Revised date: 2 June 2020
Accepted date: 26 August 2020

Please cite this article as: Chao Chen Conceptualization; Formal analysis; Methodology; Software; Validation; Writi
Philippe Duffour Conceptualization; Supervision; Writing - Review & Editing , Paul Fromme Supervision; Methodol
Modelling wind turbine tower-rotor interaction through an aerodynamic damping matrix, *Journal of Sound and Vibration* (2020), doi: https://doi.org/10.1016/j.jsv.2020.115667

Modelling wind turbine tower-rotor interaction through an aerodynamic damping matrix

Chao Chen[1*], Philippe Duffour[1] and Paul Fromme[2],

[1]Department of Civil, Environmental and Geomatic Engineering, University College London, United Kingdom

[2]Department of Mechanical Engineering, University College London, United Kingdom

[*] Corresponding author: chao.chen.15@ucl.ac.uk

Modelling wind turbine tower-rotor interaction through an aerodynamic damping matrix

Abstract

Current wind turbine modelling packages mainly adopt a complex methodology in which aerodynamic forces are coupled with the motion of the wind turbine components at every time step. This can result in long simulation run times, detrimental for the large number of simulations required for fatigue or reliability analyses. This contribution presents an efficient wind turbine modelling methodology based on blade element momentum theory and a linearization of the aerodynamic forces. This allows the wind-rotor interaction to be reduced to static forces applied at the tower top, with additional terms proportional to the tower velocities expressed as an aerodynamic damping matrix. This aerodynamic model was implemented as part of a finite element model of the tower and was successfully verified against the fully-coupled modelling package FAST. The damping matrix components explain key features of the coupling between fore-aft and side-side vibrations of the wind turbine. This coupling causes energy transfers between the two directions, complicating aerodynamic damping identification. The aerodynamic damping matrix offers novel insights and an efficient method to describe the aerodynamic damping of wind turbines.

Key words: aerodynamic damping, operating wind turbine, aerodynamic coupling, blade element momentum theory

1 Introduction

Efficient and accurate wind turbine modelling tools are necessary for the analysis and design of wind turbines. Current mainstream wind turbine modelling software packages such as FAST [1] by NREL and HAWC2 [2] by DTU describe the interaction between the tower, rotor, nacelle, and foundation of the wind turbine system by coupling aerodynamic capabilities with electromechanical and structural models. In FAST for

instance, the motions of rigid bodies (e.g. nacelle, hub) and flexible bodies (e.g. tower, blades) are coupled during the time integration, and at each time step the unsteady blade element momentum (BEM) theory [3] is used to calculate the aerodynamic loads on the rotor. Such fully coupled models are usually computationally intensive. In some cases, such as fatigue or reliability analyses, a large number of simulations is required, and a simplified approach is desirable. As a result, in some studies (e.g. [4][5][6]) the rotor-nacelle assembly (RNA) has been lumped at the top of the flexible tower and the aerodynamic interaction is modelled by applying the rotor thrust at the tower top as a point load and using a dashpot or an equivalent Rayleigh damping to represent the aerodynamic damping. Such decoupled models make it easier to include more detailed soil-structure interaction features (e.g. [4][6]) than many integrated simulation tools such as FAST currently allow. Muskulus [7] and Schafhirt and Muskulus [8] used a decoupling strategy based on a simplified rotor load model. A simple expression for the thrust, based on actuator disc theory was derived in terms of pitch angle and rotor speed by fitting a thrust coefficient to a number of fully coupled simulation results. However, the damping force in these models relied on damping coefficients obtained by fitting the response to that of an integrated simulation.

Damping is a key variable to accurately predict the dynamic response of mechanical systems. The main sources of vibration damping in a wind turbine include aerodynamic damping, structural damping, possibly supplemental damping (from devices), and soil and hydrodynamic damping in offshore turbines [9]. Aerodynamic damping is the most significant source of damping when the turbine is in operation. For structural designers it is convenient to characterise the aerodynamic damping using a linear damping ratio associated with the first vibrational mode of the tower, as this allows the dynamic response of the system to be calculated rapidly, e.g. for fatigue analyses [10]. Specific studies of the aerodynamic damping have generated experimental or analytical modal damping ratios that capture this source of dissipation [11].

Aerodynamic damping originates from the interaction between wind and rotor. The moving blades experience a drag force from the wind and this force impedes the movement of the rotor. This damping effect is implicitly included in fully coupled wind turbine modelling packages. Many studies (e.g. [11][12][13]) used these modelling packages to observe the changes in the fore-aft (FA) aerodynamic damping when the average inflow wind speeds, pitch angles, and rotation speeds are varied within relatively small ranges. Tarp-Johansen et al. [14] used HAWCStab to simulate the side-

side (SS) aerodynamic damping in a 3.5 MW Offshore Wind Turbine (OWT). They reported that whether the tower is assumed to be rigid or flexible in the FA direction affects the damping in the SS direction. This effect becomes more pronounced when the inflow wind speed is above the rated wind speed. However, due to the complexity of the system it can be difficult to isolate and quantify the aerodynamic damping from the simulation results obtained using such fully coupled software packages as it is implicitly included.

Aerodynamic damping of the tower vibrations in operating wind turbines has been measured experimentally in a number of studies, often measuring the total damping in the system. For OWTs, the aerodynamic damping values quoted below were obtained by subtracting an assumed underlying damping of 2% from the measured total damping [15]. For onshore wind turbines, the total damping is a closer approximation of the aerodynamic damping [10] as foundation damping is low. Hansen et al. [16] estimated the aerodynamic damping in a 2.75 MW operating OWT using two experimental methods. From the decay in the OWT free response, the aerodynamic damping ratios obtained were about 6% in the FA direction and 0.4% in the SS direction. Operational modal analysis (OMA) based on stochastic subspace identification (SSI) was also used to extract the damping ratios while the turbine is subjected to wind excitation, resulting in an aerodynamic damping ratio of 11% for the FA direction and 6% in the SS direction. Ozbek and Rixen [13] directly estimated the aerodynamic damping in an operating 2.5 MW onshore turbine using OMA. Photogrammetry and laser vibrometry were used to measure the vibration response, and the damping ratios were obtained by the least square complex exponential (LSCE) method. Their measured damping values, averaging around 5% in the FA direction and 0.5% in the SS direction, were in good agreement with results from HAWCS simulations they carried out. Koukoura et al. [17] used Enhanced Frequency Domain Decomposition (EFDD) to estimate the damping in an 3.6MW operating OWT and obtained overall damping ratios of 10% and 5% in the FA and SS directions respectively. These values are unusually high, probably due to the presence of supplemental damping devices, which are mentioned but whose effect has not been specified. Weijtjens et al. [18] and Hu et al. [19] both implemented the poly least-squares complex frequency-domain (p-LSCF) method to identify the total damping in operating 5 MW and 3 MW wind turbines respectively. For different wind speeds from 1.5 m/s to 22.7 m/s, Weijtjens et al. obtained values in the range of 1.8% to 6.5-7% for the FA direction and 1.8% to 3% in the SS direction, while Hu et al.

obtained averaged total damping ratios in the range of 0.5% to 4% for an onshore operating wind turbines with rotor rotation speeds between 4 rpm to 15 rpm (direction of vibration not specified). Dong et al. [20] and Dai et al. [21] applied similar modified SSI methods to identify the frequency and damping in operating turbines, and the modification improves classic SSI when the excitation contains harmonic forces. More detailed discussion of damping identification in operating wind turbines can be found in [22].

Aerodynamic damping has also been calculated directly. Salzmann and Tempel [12] summarised several theoretical expressions for aerodynamic damping in the FA direction for constant-speed turbines, including the methods by Garrad [23] and Kühn [24], additionally proposing an analytical model for variable-speed turbines. They obtained closed-form expressions that account for the relationship between wind speed and the motion of the turbine, based on BEM theory. Valamanesh and Myers [11] proposed a semi-analytical solution also based on BEM theory that predicts the aerodynamic damping in both FA and SS directions. They compared their prediction to results from FAST simulations for a range of settings that cannot be captured easily using the BEM derivation, such as the presence of wind shear and shaft tilt. Generally, their results agree well with FAST and they found that the assumption of rigid blades has the largest impact on the damping values, but only reduces the damping estimates by an average of 1% (in relative change). Chen et al. [25] presented a wavelet-based approach that can continuously identify the aerodynamic damping for an operating wind turbine. Using a lumped-mass model of the wind turbine and BEM theory, simulated time series for turbulent wind were analysed in the time-frequency domain and the long-time variation of the aerodynamic damping matrix was estimated. Liu et al. [26] developed a model to calculate FA aerodynamic damping in a similar form to the model proposed by Kühn [24], but a correction factor was introduced, so that the aerodynamic damping in a variable-speed wind turbine can be considered. Chen and Duffour [22] derived analytical solutions for uncoupled FA and SS aerodynamic damping factors using first order Taylor expansion to linearize the aerodynamic loads. The available studies on aerodynamic decoupling and damping mainly concentrate on aerodynamic damping in the FA direction and usually do not take into account the interaction between FA and SS motions. However, the FA and SS motions are coupled, and the wind turbine vibrates in both directions simultaneously. In this paper, we investigate the nature of this coupling using a BEM-based analytical derivation of the

aerodynamic damping and show that it can be represented through a non-standard damping matrix. Petersen et al. [27] also used a similar non-standard damping matrix to represent the aerodynamic damping in operating wind turbines, but focussed on blade vibrations. The vibration behaviour of the coupled system is complex and significant limitations in the conventional description of the aerodynamic damping by one or two modal damping ratios (FA and SS) were identified. Energy transfers take place between the FA and SS motions and this has to be carefully accounted for the accurate characterisation of the tower damping. This paper is structured as follows. Section 2 describes the vibration problem caused by the coupling between FA and SS motions and gives the motivation for this study. Section 3 describes the decoupling methodology and the derivation of the damping matrix. Section 4 verifies the results from the developed methodology against FAST simulation results and discusses useful limit cases. The behaviour of the proposed damping matrix as compared to a conventional aerodynamic damping description (decoupled model) is illustrated and discussed for the variation of the wind speed. Section 5 concludes the paper.

2 **Problem statement**

The coupling between FA and SS motions is illustrated in this section using simulation results from a fully coupled wind turbine model of the NREL reference three-blade onshore wind turbine available in FAST [28]. The settings used for these simulations are described in Section 4. The main properties of this wind turbine model are listed in Table 1. The dynamics of the tower in FAST is modelled as the superposition of the first two SS and FA bending modes.

Table 1. Basic Properties of the modified NREL 5MW reference onshore wind turbine.

Rotor Diameter, R	126m
Hub Height	87.6m
Tower Diameter, D	3.87-6.00m
Tower Thickness, t	19-27mm
Lumped Mass at Top	3.5×10^5 kg
Rated Wind Speed	12.1m/s
Natural Frequency	0.34 Hz

Figure 1 shows the simulated tower top FA (a) and SS (b) displacements time histories using the FAST software. The responses were obtained for a 1m initial displacement in the FA direction of the tower top while the turbine is operational at a steady-state wind speed of 20m/s. No initial displacement was given in the SS direction. Two types of dynamic response were considered. In one case, the system was free to move both in the FA and SS degrees of freedoms (DOFs) (solid lines). For the second case (dashed lines), the system was only permitted to move in the FA direction, considering the SS DOF as rigid (by switching the corresponding DOF off in FAST). The wind speed, rotor rotation speed (12.1rpm) and pitch angles (17.6°) of the blades were kept constant at the nominal values during the simulation.

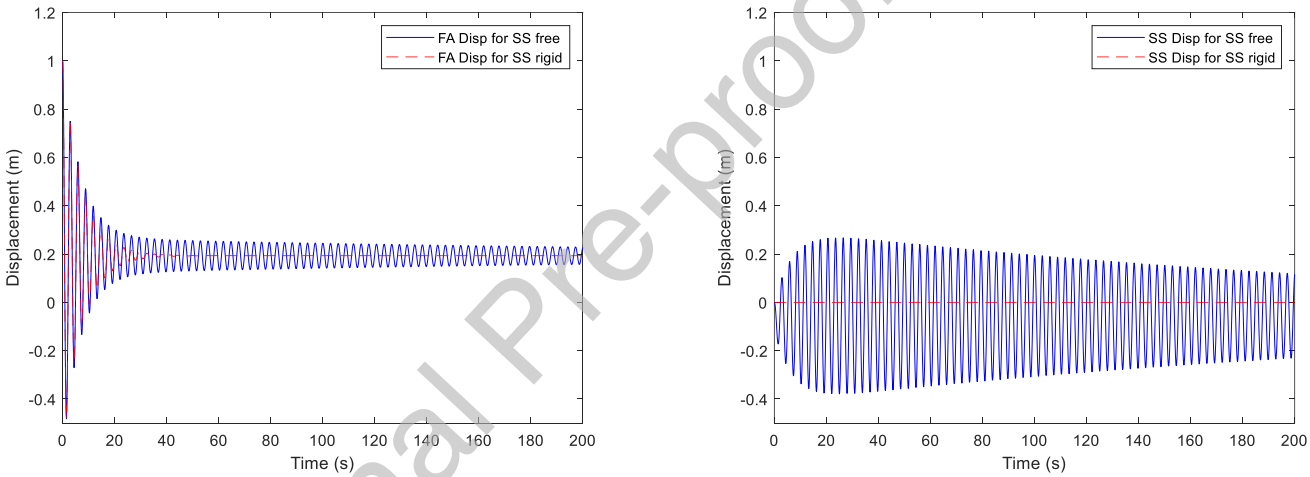

(a) (b)

Figure 1. Tower top displacements in the FA (a) and SS (b) directions simulated using FAST with SS direction free (solid) or kept rigid (dashed).

Figure 1(a) shows that the SS motion influences the FA motion damping, as can be seen from the slower FA response decay in the solid curve (SS free) compared to the dashed curve (SS rigid). Such an apparent change in damping in the FA direction could have a significant effect in fatigue analyses. Figure 1(b) shows that even without any initial displacement in the SS direction, a sideway response at the tower top is excited, growing initially as energy is transferred from the FA direction, before gradually decreasing. This coupling effect is due to the aerodynamic forces on the rotor in the two directions. When the tower bends, the rotor plane moves and is no longer perpendicular to the incoming wind. This causes unbalanced resultant forces in the SS and vertical

directions as well as unbalanced moments, which cause static deflections and oscillations. Conversely, the SS motion affects the FA motion and causes the damping to undergo an apparent change over time: the FA amplitude does not decay with a simple exponential envelope: it reduces at a fast rate initially but then decays at a much slower rate after 25s (in the case shown in Figure 1, SS free). This leads to very different apparent decay rates and therefore damping values depending on which part of the curve is analysed. The details of this coupling depend on the inflow wind speed, pitch angle, and rotor speed, and for different combinations of these parameters, the vibration response may look slightly different as demonstrated in Section 4. This study was motivated by these observations. The intention is to propose an efficient methodology allowing the dynamics of the coupled system to be modelled without the requirement of unsteady aerodynamic simulations and to better characterize and understand how the aerodynamic damping affects the behaviour of wind turbines.

3 **Methodology**

3.1 **Description of the model**

Key features of the dynamic response of a wind turbine tower can be captured by modelling it as a cantilevered beam with a lumped mass connected to the free end [19]. The lumped mass at the top represents the RNA mass and the beam accounts for the wind turbine tower as shown in Figure 2. During normal operation, the rotor is subjected to the loads from the inflow wind, and the whole wind turbine is excited and vibrates. Excluding non-aerodynamic sources of dissipation, the vibration of the tower is damped by the wind-structure interaction – mainly the wind-rotor interaction, although the wind-tower interaction also has a small contribution. As the tower is axisymmetric and the RNA is lumped at the top, motions in the two directions cannot be coupled through a stiffness mechanism and our results confirm this. In the model presented here, the aerodynamic loads are separated into two parts: the aerodynamic load on a rigid tower/rotor and the aerodynamic damping force captured through a viscous damping matrix. The details of the tower modelling and the aerodynamic damping matrix are given in Sections 3.2 and 3.3. The turbine model is based on the modified NREL 5 MW reference onshore wind turbine (Table 1), assuming the tower

is clamped at ground level. To simplify the model and limit the number of variables necessary to describe the system, the following modelling assumptions were made:

1. The connections between the tower top (or yaw bearing in FAST), the nacelle, and the rotor are considered rigid. This means that the displacement, velocity and acceleration of the rotor centre can be described as a combination of the translational and rotation of the tower top. Vertical displacements and the rotation about the vertical axis were considered negligible compared to lateral motions.
2. The rotor blades are rigid so blade flapwise and edgewise vibrations are not considered. This means that the relative wind speed experienced by each blade element is only influenced by the inflow wind speed, the RNA linear/angular velocity and the rotation speed of the rotor. The permanent shaft tilt and blade precone angle were set to zero.
3. The RNA velocity is much smaller than the inflow wind speed and the speed of the blade elements due to rotor rotation. This allows the aerodynamic forces to be linearized using first order Taylor expansion.

3.2 **Finite element modelling of the tower**

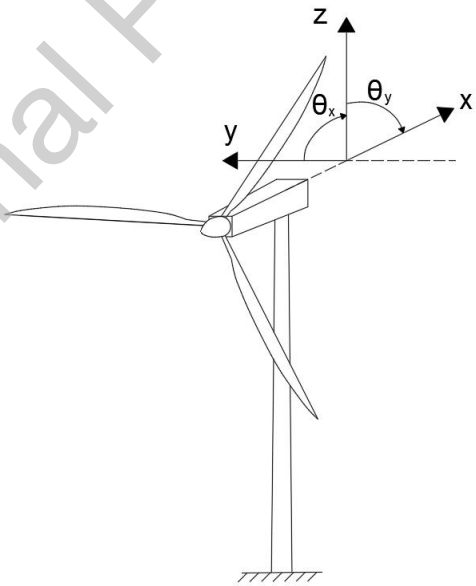

Figure 2. Schematic of the wind turbine.

The wind turbine was modelled using a bespoke finite element (FE) code written in MATLAB. The tower was modelled using 11 Euler-Bernoulli beam elements of equal length. Each node can translate and rotate in two perpendicular directions as shown in

Figure 2. x (FA) and y (SS) denote translations while θ_x and θ_y denote rotations about the x and y axes respectively. For a vibrating system, the equations of motion can be expressed in matrix form:

$$\mathbf{M}\ddot{\mathbf{u}}(t) + \mathbf{C}\dot{\mathbf{u}}(t) + \mathbf{K}\mathbf{u}(t) = \mathbf{F}(t), \quad (1)$$

where $\mathbf{M}$, $\mathbf{K}$ and $\mathbf{C}$, are the mass matrix, stiffness matrix, and damping matrix respectively, $\mathbf{u}(t)$ is the displacement vector, and $\mathbf{F}(t)$ is the external force vector. The lumped mass representing the RNA was added to the relevant terms in the mass matrix for the top node of the tower. The moments of inertia of the RNA were set to zero to allow for a like-for-like comparison with FAST model output. This will be further discussed in Section 4.1. The mass and stiffness matrices can be easily formed for each element, using the material and geometric properties of the tower. Structural damping could be added as Rayleigh damping to this model, but zero structural damping was assumed throughout so that the aerodynamic damping is the only damping source. The time integration algorithm used to solve the equation of motions in Equation (1) in the time domain is HHT-α [20] – a generalised version of the widely-used Newmark-β method.

3.3 Theoretical derivation of the aerodynamic damping matrix

3.3.1 Formation of basic equations for aerodynamic loads

As mentioned in Section 3.1, the rotor is assumed to be rigidly connected to the tower top. In BEM theory, the calculated aerodynamic loads are related to the relative wind speeds experienced by each blade element. Therefore, it is necessary to determine the velocity of each blade element caused by the combined translation and rotation of the rotor.

It is assumed that the rotor is facing an inflow wind of steady velocity V_0 pointing in the positive direction of the x axis, as indicated in Figure 3. The rotor rotates positively clockwise around the x axis at a speed ω so that a blade element at distance r along the blade length moves at a speed $V_r = \omega r$ perpendicular to the blade and tangential to the circular path described by the blade element at r as it rotates. The azimuthal angle $\gamma(t)$ indicates the azimuthal position of the blade. The FA motion of the tower produces a tower top linear velocity $\dot{x}$ and an angular velocity $\dot{\theta}_y$. The SS motion of the tower leads to a linear velocity $\dot{y}$ and an angular velocity $\dot{\theta}_x$. These velocities cause small variations

in the relative wind speeds experienced by blade elements. For an arbitrary blade element at distance r from the hub centre with azimuthal position $\gamma(t)$, the relative wind speed experienced in the normal direction, V_{xRel}, can be written as

$$V_{xRel} = V_0 - \dot{x} - \dot{\theta}_y r cos\gamma(t), \tag{2}$$

and the relative wind speed in tangential direction, V_{rRel}, is

$$V_{rRel} = V_r - \dot{y} cos\gamma(t) + \dot{\theta}_x r. \tag{3}$$

V_{rRel} is tangential to the trajectory of the blade element as it rotates around the hub axis, perpendicular to the radial direction of a blade in the rotor plane. A positive V_{xRel} is a velocity toward the positive direction of the x axis, while a positive V_{rRel} is a velocity having the opposite sign to the rotor rotation speed. In Equations (2) and (3), $\dot{x}$, $\dot{y} cos\gamma(t)$, $\dot{\theta}_y r cos\gamma(t)$ and $\dot{\theta}_x r$ are caused by the motion of the tower top.

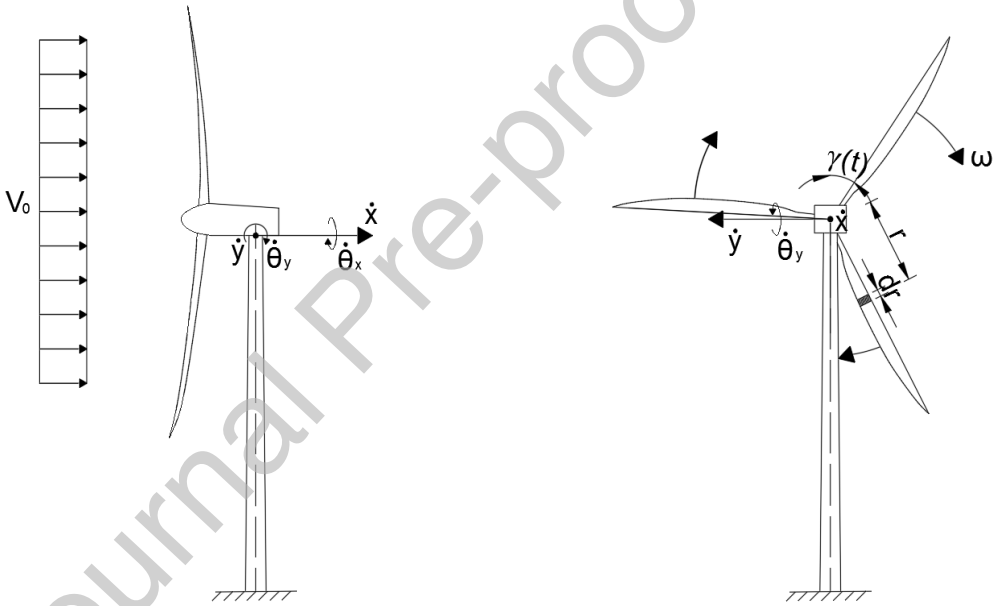

(a) (b)

Figure 3. Fore-aft (a) and side-side (b) motions.

The angular velocity $\dot{\theta}_y$ is assumed to cause the whole rotor to simply rotate around the hub, therefore the resultant linear velocities of the blade elements above the hub have inverse signs compared to those below the hub. As a result, the relative velocity caused by $\dot{\theta}_y$ can be calculated as $\dot{\theta}_y r cos\gamma(t)$.

The next step is to find the force and moment expressions of a single blade element for the relative wind velocities in Equations (2) and (3). The coordinate system used for the resultant forces and moments is consistent with the motion coordinates shown in

Figure 2. Assuming that the tower is rigid, the steady-state forces in normal and tangential directions applied to one blade element are denoted $dT(V_0, V_r)$ and $dS(V_0, V_r)$ respectively. When the tower is flexible, assuming the changes in relative wind speed experienced by every blade element are sufficiently small, the aerodynamic loads considering the tower top motion can be obtained using a first order Taylor expansion of the forces around the steady-state normal and tangential wind velocities. Effectively, this linearizes the aerodynamic forces in terms of velocity.

The force in the normal direction is given by:

$$\begin{aligned} &dT(V_{xRel}, V_{rRel}) \\ &\quad = dT(V_0, V_r) + \frac{\partial(dT)}{\partial V_0}(-\dot{x}) + \frac{\partial(dT)}{\partial V_0}\left(-\dot{\theta}_y r cos\gamma(t)\right) \\ &\quad + \frac{\partial(dT)}{\partial V_r}(-\dot{y} cos\gamma(t)) + \frac{\partial(dT)}{\partial V_r}\left(\dot{\theta}_x r\right); \end{aligned} \tag{4}$$

and the force in the tangential direction is given by:

$$\begin{aligned} &dS(V_{xRel}, V_{rRel}) \\ &= dS(V_0, V_r) + \frac{\partial(dS)}{\partial V_0}(-\dot{x}) + \frac{\partial(dS)}{\partial V_0}\left(-\dot{\theta}_y r cos\gamma(t)\right) \\ &\quad + \frac{\partial(dS)}{\partial V_r}(-\dot{y} cos\gamma(t)) + \frac{\partial(dS)}{\partial V_r}\left(\dot{\theta}_x r\right). \end{aligned} \tag{5}$$

The moment about the y direction is given by:

$$\begin{aligned} &dM_y(V_{xRel}, V_{rRel}) = dT(V_{xRel}, V_{rRel}) r cos\gamma(t) \\ &= dT(V_0, V_r) r cos\gamma(t) + \frac{\partial(dT)}{\partial V_0}(-\dot{x}) r cos\gamma(t) + \frac{\partial(dT)}{\partial V_0}\left(-\dot{\theta}_y r^2 cos^2\gamma(t)\right) \\ &\quad + \frac{\partial(dT)}{\partial V_r}(-\dot{y} r cos^2\gamma(t)) + \frac{\partial(dT)}{\partial V_r}\left(\dot{\theta}_x r^2 cos\gamma(t)\right); \end{aligned} \tag{6}$$

and the moment about the x direction is given by:

$$\begin{aligned} &dM_x(V_{xRel}, V_{rRel}) = dS(V_{xRel}, V_{rRel}) r \\ &= dS(V_0, V_r) r + \frac{\partial(dS)}{\partial V_0}(-\dot{x}) r + \frac{\partial(dS)}{\partial V_0}\left(-\dot{\theta}_y r^2 cos\gamma(t)\right) \\ &\quad + \frac{\partial(dS)}{\partial V_r}(-\dot{y} r cos\gamma(t)) + \frac{\partial(dS)}{\partial V_r}\left(\dot{\theta}_x r^2\right). \end{aligned} \tag{7}$$

The total forces and moments applied to the rotor are obtained by summing the elemental forces and moments along the three blades. As $\sum_1^{N_b} cos\gamma(t) = 0$ for any t, the total force in the x (FA) direction is:

$$F_x = \sum_1^{N_b} \int_0^R dT(V_{xRel}, V_{rRel}) \\ = N_b \int_0^R dT(V_0, V_r) - \dot{x} N_b \int_0^R \frac{\partial(dT)}{\partial V_0} + \dot{\theta}_x N_b \int_0^R r \frac{\partial(dT)}{\partial V_r}, \quad (8)$$

where N_b is the number of blades, and R is the radius of the blade.

The total force in the y (SS) direction is:

$$F_y = -cos\gamma(t) \sum_1^{N_b} \int_0^R dS(V_{xRel}, V_{rRel}) \\ = \dot{\theta}_y \frac{N_b}{2} \int_0^R r \frac{\partial(dS)}{\partial V_0} + \dot{y} \frac{N_b}{2} \int_0^R \frac{\partial(dS)}{\partial V_r}. \quad (9)$$

The negative sign on the left-hand side of the summation operator is due to the fact that for a rotor rotating positively, the blade at a position above the hub is subjected to a tangential force towards the negative y-direction. This is a consequence of the chosen coordinate system. In addition, it can be easily checked that for a three-blade wind turbine, $\sum_1^{N_b} cos^2\,\gamma(t) = N_b/2$.

Eventually, the total moment about the y axis is:

$$M_y = \sum_1^{N_b} \int_0^R dM_y(V_{xRel}, V_{rRel}) \\ = -\dot{\theta}_y \frac{N_b}{2} \int_0^R r^2 \frac{\partial(dT)}{\partial V_0} - \dot{y} \frac{N_b}{2} \int_0^R r \frac{\partial(dT)}{\partial V_r}, \quad (10)$$

whereas the total moment about the x axis is:

$$M_x = \sum_1^{N_b} \int_0^R dM_x(V_{xRel}, V_{rRel}) \\ = N_b \int_0^R dS(V_0, V_r) r - \dot{x} N_b \int_0^R r \frac{\partial(dS)}{\partial V_0} + \dot{\theta}_x N_b \int_0^R r^2 \frac{\partial(dS)}{\partial V_r}. \quad (11)$$

Appendix A provides analytical expressions allowing the partial derivatives in Equations (8) to (11) to be calculated in terms of blade characteristics and operating conditions.

3.3.2 **Aerodynamic load resultants at the tower top**

Within the set of assumptions made, the rotor aerodynamic load resultants at the hub are completely described by Equations (8) to (11), and these loads can be separated into two parts: static (constant) components and "damping" components proportional to the

velocities. Only F_x and M_x have a static part equal to $N_b \int_0^R dT(V_0, V_r)$ and $N_b \int_0^R dS(V_0, V_r) r$ respectively. These can easily be calculated using the steady BEM model in MATLAB or FAST by keeping the tower rigid. They can then be applied as external loads at the tower top in a decoupled model. The other terms in F_x, F_y, M_x and M_y appear as damping components since they depend linearly on the tower top translational or angular velocities. These damping components can be added to the relevant terms for the top node in the damping matrix of the overall system. A separate aerodynamic damping matrix $\mathbf{C}_{Aero}$ that collects the terms multiplied by the velocity vector $\dot{\mathbf{u}} = \left[\dot{x}\, \dot{y}\, \dot{\theta}_x\, \dot{\theta}_y\right]^T$ for the top node can be defined as:

$$\mathbf{C}_{Aero}\dot{\mathbf{u}} = \begin{bmatrix} N_b \int_0^R \frac{\partial(dT)}{\partial V_0} & 0 & -N_b \int_0^R r \frac{\partial(dT)}{\partial V_r} & 0 \\ 0 & -\frac{N_b}{2} \int_0^R \frac{\partial(dS)}{\partial V_r} & 0 & -\frac{N_b}{2} \int_0^R r \frac{\partial(dS)}{\partial V_0} \\ N_b \int_0^R r \frac{\partial(dS)}{\partial V_0} & 0 & -N_b \int_0^R r^2 \frac{\partial(dS)}{\partial V_r} & 0 \\ 0 & \frac{N_b}{2} \int_0^R r \frac{\partial(dT)}{\partial V_r} & 0 & \frac{N_b}{2} \int_0^R r^2 \frac{\partial(dT)}{\partial V_0} \end{bmatrix} \begin{bmatrix} \dot{x} \\ \dot{y} \\ \dot{\theta}_x \\ \dot{\theta}_y \end{bmatrix}. \tag{12}$$

$\mathbf{C}_{Aero}$ can be written more concisely:

$$\mathbf{C}_{Aero} = \begin{bmatrix} c_{xx} & 0 & c_{x\theta_x} & 0 \\ 0 & c_{yy} & 0 & c_{y\theta_y} \\ c_{\theta_x x} & 0 & c_{\theta_x \theta_x} & 0 \\ 0 & c_{\theta_y y} & 0 & c_{\theta_y \theta_y} \end{bmatrix}. \tag{13}$$

$\mathbf{C}_{Aero}$ has a number of relevant structural features:

1) For given inflow wind speed, rotation speed, and pitch angle, the coefficients in the damping matrix are constant and can therefore be calculated using a steady BEM model before time integration. Therefore, the proposed strategy allows the vibration and aerodynamics to be decoupled in the sense that the aerodynamic calculation can be done once, for a given range of steady-state operating conditions regimes. Changes of the damping matrix due to unsteady wind inflow are not considered in the main body of the paper, but the effects of this unsteadiness and blade flexibility on observed damping were assessed in Appendix B from FAST simulations. Further investigation on how to incorporate these for accurate damping and vibration behaviour prediction should be conducted.

2) From the structure of this damping matrix, it can be seen that the translational DOFs in the FA and SS are not coupled. Coupling between FA and SS directions only occurs through the off-diagonal terms linking rotational to translational DOFs. For example, $c_{x\theta_x}$ links the FA translational velocity $\dot{x}$ to the rotation around the x-axis $\dot{\theta}_x$.
3) When the tower is assumed as rigid in the SS direction, two diagonal terms c_{xx} and $c_{\theta_y\theta_y}$, contribute to the damping in the FA direction, which means that both linear and angular motions contribute to the aerodynamic damping in that direction. A similar observation can be made in the SS direction. Coupling would not occur if the tower top rotation was not considered.
4) An important feature of this aerodynamic damping matrix is that although it has clear structural patterns, it is not symmetric. This is not uncommon when considering damping in rotating machineries [21]. It should be remembered that this matrix was derived from the linearization of the aerodynamic forces rather than from conventional dashpots located within a standard multiple DOF system.
5) Only the symmetric part of this matrix represents genuine energy dissipation. The anti-symmetric part couples the DOFs without contributing to the overall damping of the system. Any damping matrix $\mathbf{M}$ can be decomposed into a symmetric part $\mathbf{S}$ and an antisymmetric part $\mathbf{A}$ such that $\mathbf{M} = \mathbf{S} + \mathbf{A}$.

The expressions defining this aerodynamic damping matrix allow a better understanding of the nature of the coupling between FA and SS motions and the aerodynamic forces. The complete derivation described in this section and Appendix A provides a model from which the dynamic response for an operational wind turbine can be rapidly calculated. This is particularly useful when calculating the responses of a wind turbine using a more detailed foundation model, which cannot be easily coupled with an aerodynamic rotor model. In this case, the aerodynamic damping is typically defined separately as damping ratios in the FA and SS directions. The aerodynamic damping matrix defined here provides another option which more accurately captures the interaction between the FA and SS motions. In addition, the damping matrix could be used to underpin an experimental methodology to identify the dynamic properties of the system from experimental data. In contrast to conventional operational modal analysis which gives modal damping factors for a structural system (e.g. [32][17][33]),

damping identification in operational wind turbines could aim to quantify the terms of the aerodynamic damping matrix (e.g. using a time-frequency analysis such as that proposed by Chen et al. [15]).

4 Results and discussion

4.1 Model verification and overall behaviour

4.1.1 FAST model settings for verification

FAST was used to verify the results from the proposed model. In contrast to the default settings in FAST, the centre of mass of the RNA was moved to the tower top and the moments of inertia of the RNA relative to the tower top were set to zero. This modification was necessary to make the FAST model consistent with the one used here. In principle this should not be necessary, but it is not clear how to define different RNA moments of inertia in the x and y directions in FAST, so they were set to zero. FAST also requires the tower mode shapes as an input and these were obtained from an eigenfrequency analysis of the FE model. For consistency with the derivations presented in Section 3, the settings "classic BEM theory with the Prandtl and Glauert's corrections" were chosen in FAST's AeroDyn module [25].

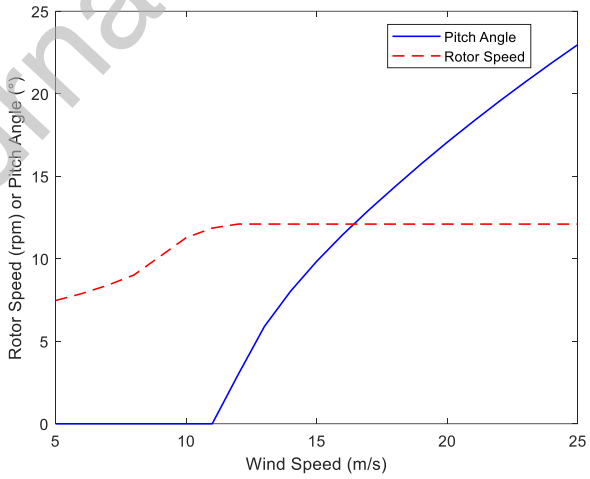

Figure 4. Standard relationship between the rotor speed (dashed), pitch angle (solid) and inflow wind speed, based on [28].

To consider the influence of the control system and obtain plausible wind turbine responses for varying normal operating conditions, the standard relationships between

wind speed, rotor speed, and pitch angle were used as shown in Figure 4 [28]. In the following FAST simulations, the wind turbine was excited dynamically by giving the tower top an initial unit (1 m) displacement in the FA direction on top of its steady-state response due to constant and uniform incoming wind field. The rotor speed, pitch angle, and inflow wind speed were kept constant during each simulation.

4.1.2 **Verification and general description of the response**

In the proposed model, the static components of the loads were calculated using Equations 8-12 and applied as external forces and moments. An initial displacement of 1m in the FA direction was then given to the tower top node to excite dynamic responses comparable to the FAST results. Figure 5 shows the time domain responses generated by the proposed model and the corresponding FAST simulation results for two wind velocities – one below the rated speed: 10m/s (Figure 5 (a) and (b)) and one above the rated speed: 20m/s (Figure 5 (c) and (d)). The agreement between the two models is very good and similar agreement was obtained at all other wind speeds. Comparing the damped responses from the proposed model to that from FAST, small percentage differences in frequency and dynamic amplitude, of up to 1% and 5% respectively, can be observed. These small differences can be explained by the simplifying assumptions underpinning the proposed model (linearization of forces; no vertical displacement or rotation; resultant forces calculated on undeformed geometry, decoupled time integration).

The consistently good agreement obtained confirms that the model adequately captures the underlying physics to the same level of accuracy as FAST. This also confirms that the coupling between the two directions is indeed caused by the off-diagonal terms of the damping matrix and not by stiffness coupling (as there is none in the model).

Figure 5 shows that the overall response of the coupled system following an initial FA displacement is a decaying oscillation in the FA direction whereas in the SS direction an oscillation initially grows from zero and then slowly decays. Both oscillations slowly converge to their respective non-zero steady-state static displacement values, which depend on the operating conditions. The decays are not simply exponential, making the use of standard damping estimation techniques problematic. The overall SS behaviour looks similar regardless of the wind speed (although the amplitude does depend on it); however, the FA response changes with the wind speed: below the rated speed (11 m/s),

the decay envelope of the response decreases to almost zero (at around 25s in Figure 5(a)) before increasing slightly again, whereas above the rated wind speed the envelope decreases monotonically. This type of behaviour was observed experimentally by Devriendt et al. [35]. As observed in Section 2 (Figure 1(a)), regardless of the wind speed, this envelope is never a simple exponential decay.

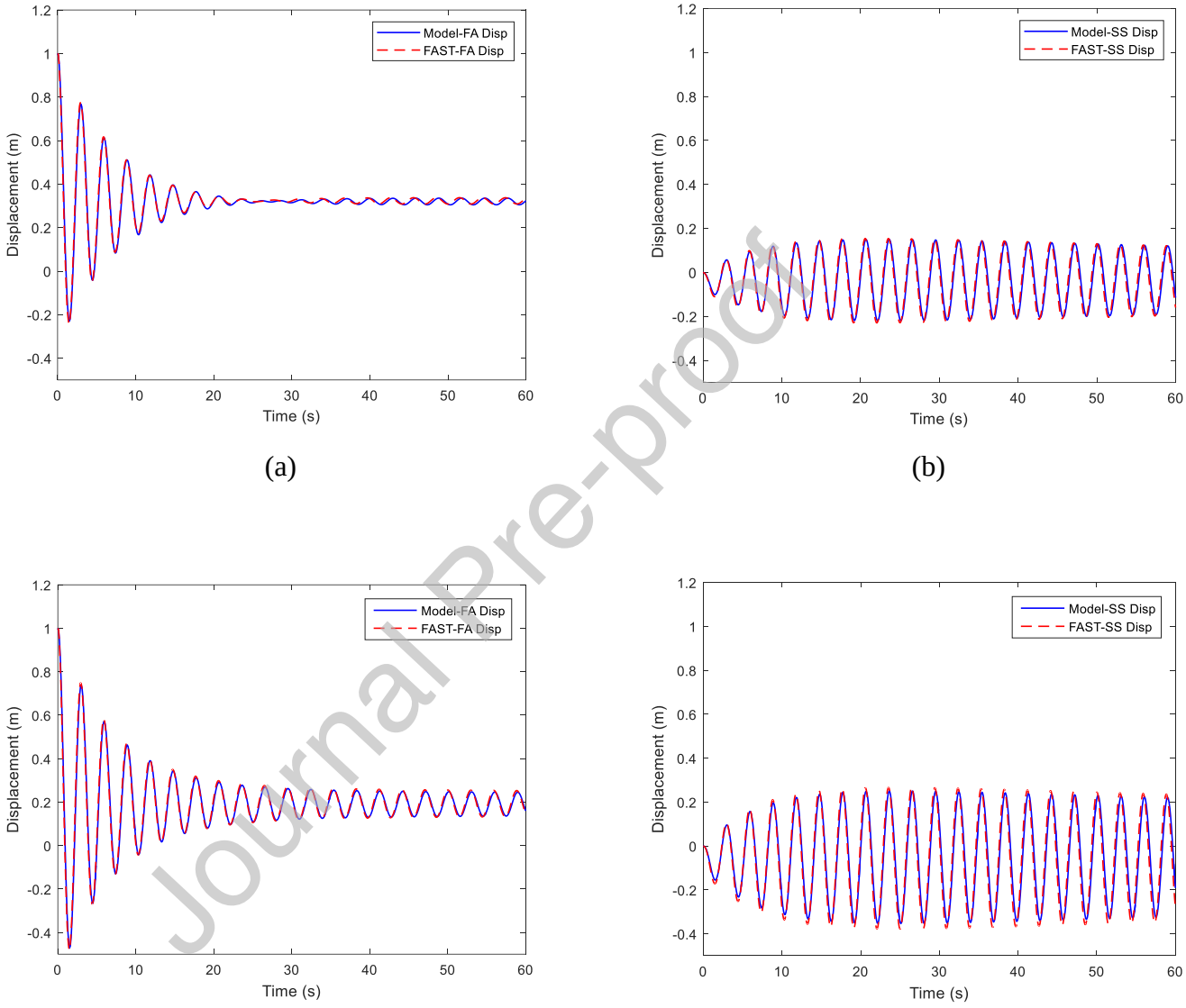

Figure 5. FA (a, c) and SS (b, d) displacement response caused by a 1m initial displacement in the FA direction; Comparison between proposed model and FAST for steady wind speeds of (a-b) 10m/s, (c-d) 20m/s.

The validity of a number of assumptions was tested, especially the assumption of rigid blades for the derivation of the damping matrix. The influence of the flexibility of the

blades was studied using FAST simulations with distributed rotor inertia and flapwise and edgewise blade bending modes enabled. This is shown in Figure 6 for a mean wind speed of 20m/s and a 1m initial displacement in the FA direction at tower top.

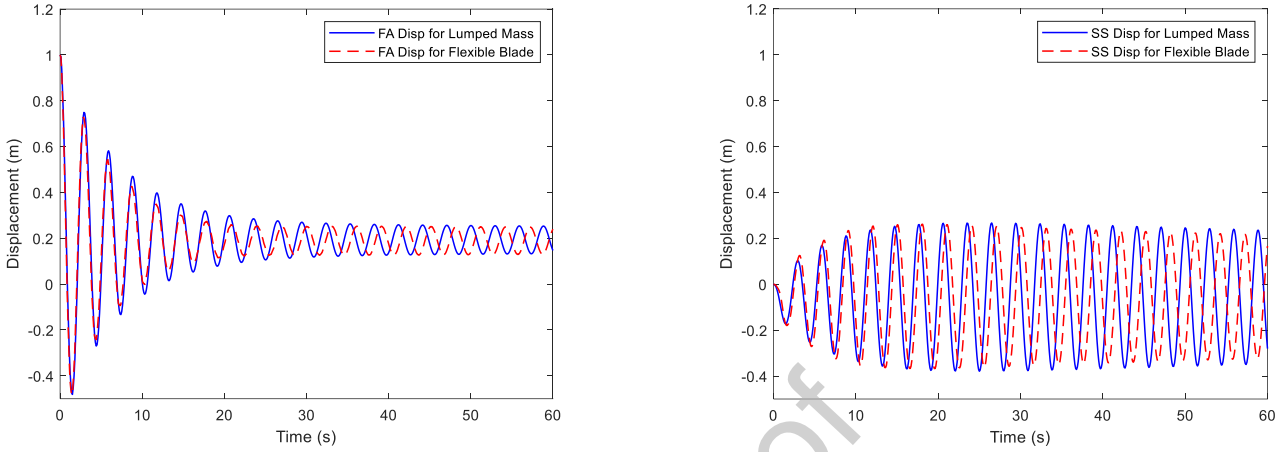

(a) (b)

Figure 6. FA (a) and SS (b) displacement response caused by a 1m initial displacement in the FA direction; Comparison between FAST models with a lumped mass, flexible blades for steady wind speeds of 20m/s

From this comparison, the natural frequency of the first tower bending modes has shifted by 3% between the two models (0.34 Hz for the lumped RNA, 0.33 Hz for the flexible blades). This is due to the distribution of the blade masses and the inclusion of blade motions. Similar responses in the FA and SS directions can be seen, with slightly higher decay rates for the flexible blade model, in line with the conclusions by Valamanesh and Myer [11]. The model developed in Section 3 does not consider unsteady or non-uniform inflow wind fields, the effect of this in combination with flexible blades on the damping estimation is discussed in Appendix B.

In addition to the flexibility of the blades, the effect of a non-zero static shaft tilt and blade precone were also tested using additional FAST simulations, where the shaft tilt and the precone were set to -5° and 2.5° respectively. This confirmed that these two parameters have negligible influence on the aerodynamic damping. Other simulations including wind shear of the incoming wind field and tower shading were also conducted to test the influence of 1P and 3P excitation. Results (not shown) confirmed that these effects have no significant effect on the aerodynamic damping.

4.2 **Useful limit cases**

The decoupled FE model described in Section 3 has identical mass and stiffness distributions in the FA and SS directions; therefore, the bending modes in both directions have identical natural frequencies and mode shapes (at 90^o of each other). The first three natural frequencies of the tower and RNA mass system are 0.34 Hz, 3.08 Hz and 9.16 Hz. For a standard wind load, spectral density peaks at around 0.1 Hz so that only the first bending modes will be significantly excited. The core behaviour of the system is therefore governed by two bending modes with identical natural frequencies (ignoring the asymmetry introduced by the RNA), perpendicular mode shapes, no stiffness coupling (due to symmetry), and higher damping in the FA direction than in the SS direction. A number of limit cases are considered to understand the complex behaviour of the system, considering only different parts of the full damping matrix derived in Section 3 for the time integration of the present model. To this end, it is useful to decompose the aerodynamic damping matrix, $\mathbf{C}_{Aero}$ as the sum of its symmetric part denoted by $\mathbf{C}_{Aero}^{S}$ and its anti-symmetric part denoted by $\mathbf{C}_{Aero}^{A}$. They are defined as:

$$\mathbf{C}_{Aero} = \mathbf{C}_{Aero}^{S} + \mathbf{C}_{Aero}^{A} = \begin{bmatrix} c_{xx} & 0 & c_{x\theta_x}^{S} & 0 \\ 0 & c_{yy} & 0 & c_{y\theta_y}^{S} \\ c_{\theta_x x}^{S} & 0 & c_{\theta_x\theta_x} & 0 \\ 0 & c_{\theta_y y}^{S} & 0 & c_{\theta_y\theta_y} \end{bmatrix} + \begin{bmatrix} 0 & 0 & c_{x\theta_x}^{A} & 0 \\ 0 & 0 & 0 & c_{y\theta_y}^{A} \\ c_{\theta_x x}^{A} & 0 & 0 & 0 \\ 0 & c_{\theta_y y}^{A} & 0 & 0 \end{bmatrix} \tag{14}$$

where $c_{x\theta_x}^{S} = c_{\theta_x x}^{S} = (c_{x\theta_x} + c_{\theta_x x})/2$, $c_{x\theta_x}^{A} = -c_{\theta_x x}^{A} = (c_{x\theta_x} - c_{\theta_x x})/2$, $c_{y\theta_y}^{S} = c_{\theta_y y}^{S} = (c_{y\theta_y} + c_{\theta_y y})/2$, $c_{y\theta_y}^{A} = -c_{\theta_y y}^{A} = (c_{y\theta_y} - c_{\theta_y y})/2$.

- Case 1: If the damping matrix $\boldsymbol{c}_{Aero}$ (Equations (12) and (13)) had zero off-diagonal terms, the two modes would be completely decoupled, and the system would behave like two independent single DOFs with identical natural frequencies and different damping levels. An initial FA displacement would lead to a relatively sharp decaying FA exponential response but no SS motion. A unit SS initial displacement would only produce a similar but more slowly decaying SS response, as the SS damping is much smaller than the FA damping (shown later in Figure 7).
- Case 2: The anti-symmetric components of the full damping matrix are neglected (set to zero). Then the two directions are coupled through conventional off-diagonal damping terms so that an initial FA displacement

leads to a fast decay in the FA direction, but some energy is also transferred to the SS direction which initially grows before slowly decaying. This is the overall behaviour observed in Section 4.1.2.

- Case 3: Only the off-diagonal, antisymmetric part of the full damping matrix is considered. The two modes are again coupled by the off-diagonal terms and exhibit a beating behaviour. The light antisymmetric damping causes the two otherwise identical natural frequencies to split slightly. This is apparent as a beating phenomenon whereby the oscillation in each direction is modulated in amplitude. The modulation is out-of-phase between the two directions, so that the energy is constantly transferred back and forth between the FA and the SS directions, but there is no overall dissipation.

As previously observed, the FA oscillation in Figure 5(c) decays monotonically whereas in Figure 5(a) the decay envelope of this oscillation decreases to almost zero at around 25s before increasing again. This behaviour can be interpreted as the first node of an underlying beating behaviour caused by the weak coupling introduced by anti-symmetric components of the damping matrix. For higher wind speeds, this behaviour disappears. To understand why, it is useful to look at how the coefficients of the damping matrix vary with the wind speed.

4.3 **Variation of the aerodynamic damping matrix with wind speed**

The expressions defining the aerodynamic damping matrix allow a detailed investigation of how the matrix coefficients change with the wind speed. Several effects occur simultaneously and can be observed more clearly by considering the symmetric and anti-symmetric parts of the damping matrix separately. The upper and diagonal plots in Figure 7 show the symmetric part of the full damping matrix with each subplot representing the variation of the corresponding coefficient in the matrix with wind speed. The lower left half represents the two anti-symmetric components. Missing subplots are zero coefficients.

c_{xx} and $c_{\theta_y\theta_y}$ are the diagonal terms directly contributing to the FA damping. They both follow a similar trend as can be expected from their mathematical expression (Equation (12)), increasing up to 11m/s wind speed and then plateauing at higher speeds. c_{yy} and $c_{\theta_x\theta_x}$, the diagonal terms contributing to SS damping, also follow an increasing trend (but different from the FA damping coefficients): both are almost

constant up to 11m/s wind speed, then increase steadily. The sharp change in behaviour at 11m/s is caused by the feathering of the blades which starts at that wind speed. This has been confirmed by additional simulation results without feathering (not shown). From these graphs it can be observed that blade feathering limits the FA aerodynamic damping but causes the SS damping to increase as the wind speed increases. This makes sense intuitively, as feathering turns the blades away from the inflow wind but increases their exposure in the tangential direction.

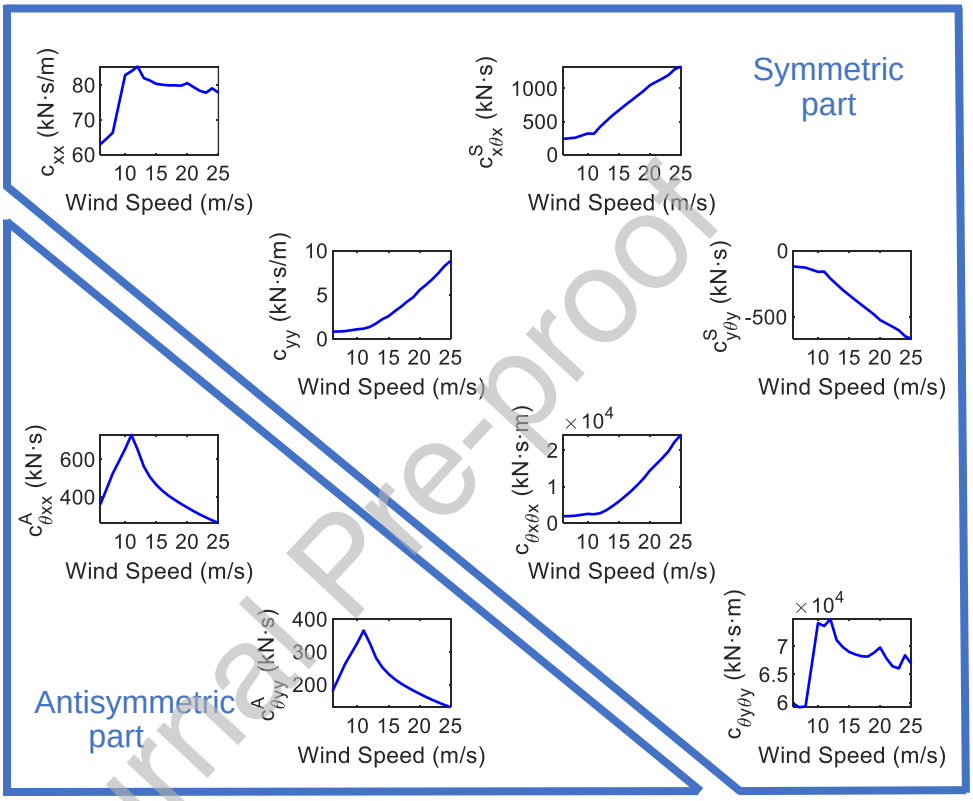

Figure 7. Coefficients of symmetric (upper) and antisymmetric (lower) parts of the damping matrix in terms of wind speed.

The symmetric off-diagonal term $c^S_{y\theta_y}$ is always negative, reasonably constant around -120kNs up to 11m/s then decreases with wind speed (increases in magnitude) down to -500kNs at 20m/s. This means that the coupling between rotation $\dot{\theta}_y$ and the SS translation y is dissipative and increases in intensity with the wind speed and feathering. By contrast the symmetric coefficient $c^S_{x\theta_x}$ is always positive, relatively constant around 250kNs up to 11m/s, then increases almost linearly to reach around 1000kNs at 20m/s. Positive values in off-diagonal terms indicate a negative damping

or positive feedback from the rotation speed $\dot{\theta}_x$ to the fore-aft translation x. This is unusual in conventional vibratory systems, but a wind turbine is not a closed system as the wind inflow constantly feeds energy in. A negative damping term indicates that the vibration coupling between the two relevant degrees of freedom transfers energy from the inflow wind into vibrational energy. From the values in Figure 7, this positive feedback is stronger than the dissipative $c^S_{y\theta_y}$ term. This explains why the system appears less damped at 20 m/s than at 10 m/s: in Figure 5(c) the FA amplitude is larger in than in Figure 5(a). As the FA amplitude is larger, the energy transferred to the SS direction is also larger. This positive feedback is presumably also the reason why in Figure 1(a), the FA amplitude is larger when both FA and SS directions are free (solid line) than when SS is rigid. In the latter case $\theta_x = 0$ so this positive feedback is not available.

Finally, both antisymmetric components decrease by about 50% from a maximum at 11m/s to 20m/s, therefore reducing the influence of the beating effect. This is indeed what is observed, as the point at which the decay envelope of the FA response decreases to almost zero before increasing again disappears at wind speeds above 11m/s.

4.4 **Comparison with conventional aerodynamic damping description for wind turbines**

The previous observations highlighted that not taking the coupling between the two directions into account could lead to erroneous damping identification. This is explored further in this section by comparing the damping in simulations considering FA and SS coupling (labelled ‘coupled’ below) or with either direction disabled (‘decoupled’).

4.4.1 **Damping ratio estimation from FRFs**

Initially, a harmonic excitation (amplitude 10kN) was applied at the tower top in either the FA or SS direction. This force is superimposed onto the wind load so a dynamic stiffness matrix cannot be straightforwardly inverted to obtain the frequency response. Time series 2000s long were generated at each forcing frequency ranging from 0.2 to 0.5Hz in 0.01Hz increments, with a smaller increment of 0.001Hz between 0.3 and 0.38Hz to increase the frequency response function (FRF) resolution near the resonance (0.34Hz). The FRFs were estimated by dividing the steady-state amplitude of the

response by that of the force. Damping ratios were estimated using the half-power bandwidth method [36].

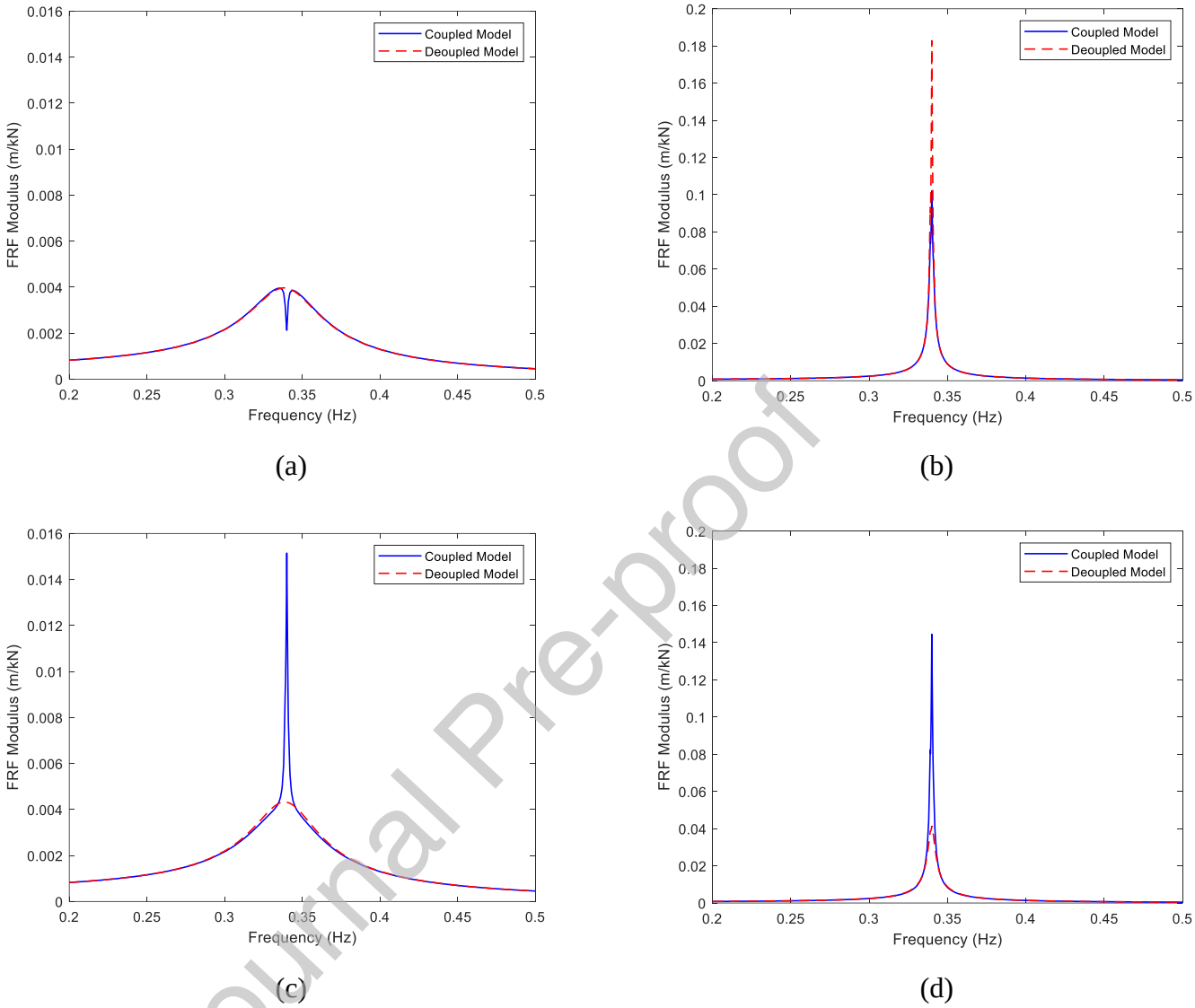

Figure 8. Modulus of the FRFs in the FA (a, c) and SS (b, d) directions for mean wind speeds of 10m/s (a, b) and 20 m/s (c, d).

Figure compares the FRFs obtained from the coupled and decoupled models for mean wind speeds at 10 m/s (Figure 8(a) and (b)) and 20m/s (Figure 8(c) and (d)). Figure 8(a) and (c) shows the FA response due to a harmonic force in the FA direction, while Figure 8(b) and (d) shows the SS response to a harmonic force in the SS direction. The decoupled responses are essentially those of a single degree of freedom system. For both wind speeds, the FA peaks are much wider that the SS peaks, indicating that the FA damping is larger (damping ratios of 6.89% for 10 m/s and 6.32% for 20 m/s) than

the SS damping ratios (0.19% for 10 m/s and 0.73% for 20 m/s), in line with literature [10].

Comparing the coupled and decoupled responses, it can be seen that the FRFs are very close at most frequencies except near resonance. Near the resonance frequency, the FA FRF curve for the coupled model at 10 m/s wind speed (Figure 8(a)) has a sharp drop, whereas for 20 m/s in Figure 8(c) the otherwise smooth coupled FRF appears to be pierced by a much sharper resonance. In the SS direction, the coupled model leads to a significantly lower (10 m/s, Figure 8(b)) or higher narrowband peak (20 m/s, Figure 8(d)), suggesting higher and lower apparent damping due to the interaction between the two directions. As the FRFs in the FA direction for the coupled model are markedly different from the FRF of a single DOF system, the use of the half-power bandwidth method to extract the damping ratios is problematic and leads to spurious results. Depending on the direction and magnitude of the sharp spike, either the estimated FA damping ratio would be almost identical to that of the decoupled model (e.g. for 10 m/s, Figure 8(a)) or dominated by the sharp spike only (e.g. for 20 m/s, Figure 8(c)), leading to an over- or underestimation of the differences between decoupled and coupled models. Therefore, it is not clear whether single damping ratios are adequate to describe the damping for the coupled model, which represents an operating wind turbine.

4.4.2 **Damping ratio estimation from decays**

As an alternative to the frequency domain method, damping ratios were estimated in the time domain using a time-frequency technique [26] on the times series obtained from a 1m initial displacement applied to the tower top in either FA or SS direction. The evaluation procedure is similar to a rotor stop test leading to an initial impulse and fitting of the decaying vibration response [35], but the turbine remains in operation throughout with a constant pitch angle. As the apparent damping value is dependent on the selection of the time window, different damping values can be obtained depending on the time window chosen for the extraction. Similar to the frequency domain method, the actual damping behaviour is being fitted to the wrong mathematical model, so there is no ideal solution to this issue. Nevertheless, the time series were more suitable to obtain damping approximations representing reasonably well the observed behaviour. For the purpose of consistency, the following procedure was followed to extract damping values: the beginning of the time window was kept at 5s, while the end of the window was gradually increased from 25s to 55s in 5s increments. Damping values

obtained for each time window were averaged to obtain the representative damping values plotted here. This procedure effectively puts more weight on the earlier part of the time series where the decay is more pronounced. Figure shows how the FA and SS damping ratios vary with wind speed depending on whether the coupling with the other direction is considered (solid) or not (dashed).

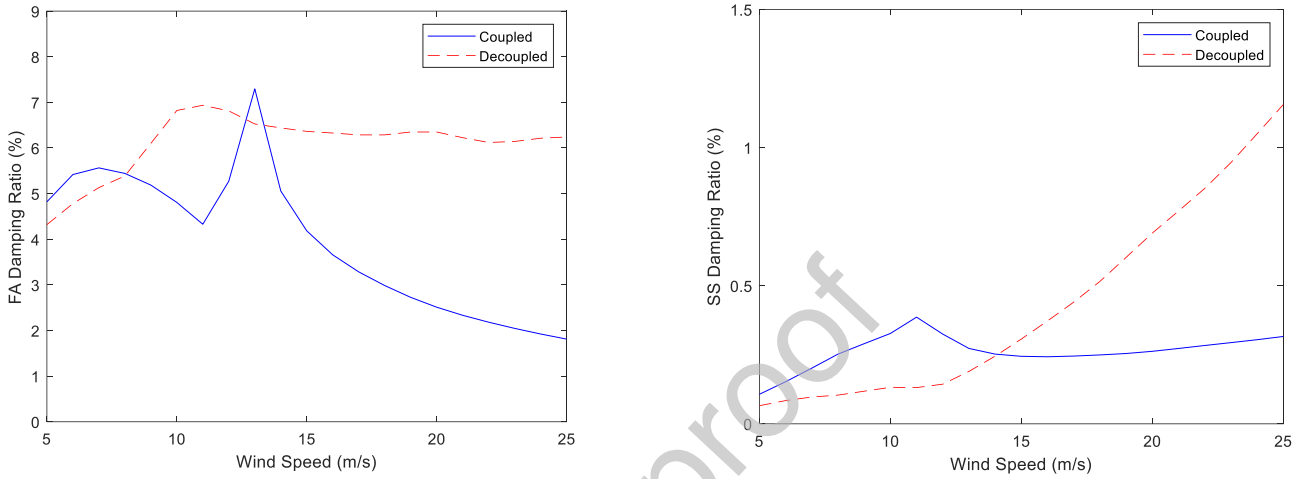

(a) (b)

Figure 9. FA (a) and SS (b) damping ratios for the first bending modes, estimated from decay in time domain. Comparisons between the model considering only one DOF (solid) and the coupled two DOFs model (dashed).

The behaviour of the decoupled system in the FA direction (Figure (a)) appears remarkably similar to the coefficients c_{xx} and $c_{\theta_y\theta_y}$ in Figure 7 and similarly the SS damping ratio of the decoupled system (Figure (b)) follows closely the evolution of coefficients c_{xx} and $c_{\theta_y\theta_y}$ with the wind speed in Figure 7. This is understandable, as the diagonal terms of the matrix represent the damping without any coupling, so they are closely linked to a system where coupling is disabled. It can be seen from Figure that the coupling between FA and SS directions has a significant influence on the damping in both FA and SS directions. Not considering the energy exchange between the two directions can lead to a large difference in the apparent damping. Considering again the wind speed of 10 m/s (below the rated wind speed), it can be seen that the sharp dip observed at the resonance frequency in the FA direction (FRF, Figure 8(a)) correlates with a reduced damping ratio as measured from the time series decay, while the decrease of the sharp peak in the FRF of the SS direction (Figure 8(b)) corresponds to increased apparent damping in the time domain. For a wind speed of 20 m/s, an

increased, sharp peak was visible in the FRFs for both directions, corresponding to a significant reduction of more than 50% for the damping ratios calculated in the time domain when the coupling between FA and SS directions is considered. It must however be noted that the damping ratios calculated from the time decay in Figure 9 must be treated with caution, as the mathematically assumed exponential decay for certain wind speeds does not match the observed time behaviour of the system. An example of this is the apparent peak in the FA damping ratio for the coupled system around 13 m/s, which is due to the vibration amplitude initially decreasing very rapidly with time and then increasing again (similar to Figure 5(a)).

Experimental measurements of tower damping ratios during operation for variation of the wind speed (similar to Figure 9) were presented in ([16][17][18][38]). The data is usually characterised by a large amount of scatter and without modelling the actual system it is difficult to make detailed comparisons, but broadly speaking the damping values published are in line with those in Figure 9. Fontecha et al. [39] compared simulation results from OpenFAST with the models proposed in [11] and [24] for their scaled experimental prototype turbine. Overall, the trend of FA damping ratios with wind speed follows a consistent pattern: an increase up to the rated wind speed followed by a plateau around 8%, similar to the decoupled system behaviour in Figure 9(a). In the SS direction, the general trend shows only a slight increase from about 0.5% up to 2% damping ratio with wind speed, similar to the coupled system behaviour in Figure 9(b).

It should be noted that based on our analytical derivations, the physics of the aerodynamic damping can be linearized and reduced to a damping matrix. However, this is not the Rayleigh damping usually assumed in experimental or operational modal analysis such as in ([16][17][18][38]), and thus cannot be captured in terms of modal damping ratios, making comparisons difficult. Simulations incorporating the blade flexibility and turbulent inflow wind fields in FAST showed a similar behaviour for the damping ratios with differences of up to about 1.35% in line with previous results for rigid blades [11], as detailed in Appendix B. Future modelling should aim to include the influence of blade flexibility on the overall vibration damping and more advanced characterization of damping to take account of the strong and unusual influence of the aerodynamic damping coupling between FA and SS directions.

5 Conclusions

This paper proposes a novel two-stage methodology that uses BEM theory to derive analytical expressions for the aerodynamic forces resultant on the rotor for steady-state operating wind turbines. In the first stage, the aerodynamic damping matrix is calculated, and in the second stage the aerodynamic damping matrix can be assigned to a FE model and its responses obtained by time integration. From these results an efficient model was developed to predict the dynamic response of the tower/RNA system. The proposed two-stage modelling strategy based on analytical derivations could be particularly well suited for fatigue and reliability analyses.

The aerodynamic forces experienced by the moving rotor are linearized and reduced to a set of resultants comprised of static terms and damping terms expressed through an aerodynamic damping matrix for constant wind speed. Both stages were implemented in MATLAB and the dynamic response was predicted using a FE model of the tower and RNA system. This model was systematically verified against an equivalent FAST model, and good agreement was obtained, confirming that the proposed model can successfully and efficiently capture the coupling effects between the FA and SS motions. The developed model does not consider the flexibility of the rotor blades and turbulent wind fields to allow for the model equations to be analytically derived. Considering aeroelasticity and turbulence can lead to a difference in damping ratios in line with literature, but does not change the strong and unusual influence of the aerodynamic damping coupling between FA and SS directions.

The closed-form expressions for the damping matrix coefficients give insight into the links between aerodynamics and the vibration response of the tower. It was shown that the key features of this response are explained by a number of characteristics of the problem:

- Due to the rotational symmetry of the tower, the two fundamental bending modes have similar natural frequencies which facilitates energy transfers between the two directions,
- Some off-diagonal coefficients of the damping matrix represent positive feedback amplifying the vibration amplitude at certain wind speeds,
- The non-symmetry of the damping matrix causes a non-dissipative coupling, apparent as a beating behaviour for certain conditions.

It was found that the apparent aerodynamic damping can be significantly influenced

by the coupling between fore-aft and side-side motions in a wind turbine, which in turn may affect the accuracy of widely-used single damping ratio techniques to describe the aerodynamic damping characteristics of wind turbines. The derived aerodynamic damping matrix could form the basis for novel damping identification techniques better suited for wind turbine systems.

Appendix A

Derivation for partial derivatives used in Section 3

This appendix gives the expressions necessary to calculate the partial derivatives defining the aerodynamic damping matrix in terms of known aerodynamic quantities such as inflow wind speed, blade profile, fluid properties and operational conditions. All notations used here are from the classic steady BEM theory [3]. These partial derivatives are $\frac{\partial(dT)}{\partial V_x}$, $\frac{\partial(dT)}{\partial V_r}$, $\frac{\partial(dS)}{\partial V_x}$ and $\frac{\partial(dS)}{\partial V_r}$. The derivation based on the variables V_0 and V_r is given. According to BEM theory, the thrust on an element at radius r can be written as

$$dT = \frac{1}{2}\rho\left[V_0^2(1-a)^2 + V_r^2\left(1+a^{'}\right)^2\right]C_n c dr, \tag{A. 1}$$

where ρ is the air density, a and $a^{'}$ are the axial and tangential induction factors respectively, c is the chord length, C_n is the normal force coefficient and dr is the increment length for this element. The tangential force can be expressed by

$$dS = \frac{1}{2}\rho\left[V_0^2(1-a)^2 + V_r^2\left(1+a^{'}\right)^2\right]C_t c dr, \tag{A. 2}$$

where C_t is the tangential force coefficient. Assuming dT and dS are functions of V_0 and V_r, other intermediate variables such as a, $a^{'}$, C_n, C_t and ϕ can also be treated as functions with regard to V_0 and V_r. ϕ is the sum of the attack angle, pitch and twist angles. According to classic BEM theory, the relationships between these variables are

$$a = \frac{1}{\frac{4\,sin^2\phi}{\sigma C_n} + 1}, \tag{A. 3}$$

where σ indicates the solidity,

$$a^{'} = \frac{1}{\frac{4sin\phi cos\phi}{\sigma C_t} - 1}; \tag{A. 4}$$

and

$$C_n = C_l cos\phi + C_d sin\phi, \tag{A. 5}$$

where C_l and C_d is the lift and drag coefficients respectively,

$$C_t = C_l sin\phi - C_d cos\phi; \tag{A. 6}$$

and

$$tan\phi = \frac{V_0(1-a)}{V_r(1+a^{'})} \; or \; cot\phi = \frac{V_r(1+a^{'})}{V_0(1-a)}. \tag{A. 7}$$

Firstly, from Equation (A. 1), $\frac{\partial(dT)}{\partial V_0}$ can be written as

$$\frac{\partial(dT)}{\partial V_0} = \frac{1}{2}\rho c \cdot dr \cdot \left[\frac{\partial(V_{Rel}^2)}{\partial V_0} C_n + V_{Rel}^2 \frac{\partial C_n}{\partial V_0}\right], \quad (A.\ 8)$$

where $V_{Rel}^2 = V_0^2(1-a)^2 + V_r^2\left(1+a^{'}\right)^2$;

$\frac{\partial(dT)}{\partial V_r}$ can be written as

$$\frac{\partial(dT)}{\partial V_r} = \frac{1}{2}\rho c \cdot dr \cdot \left[\frac{\partial(V_{Rel}^2)}{\partial V_r} C_n + V_{Rel}^2 \frac{\partial C_n}{\partial V_r}\right]. \quad (A.\ 9)$$

Similarly, from Equation (A. 2),

$$\frac{\partial(dS)}{\partial V_0} = \frac{1}{2}\rho c \cdot dr \cdot \left[\frac{\partial(V_{Rel}^2)}{\partial V_0} C_t + V_{Rel}^2 \frac{\partial C_t}{\partial V_0}\right]; \quad (A.\ 10)$$

and

$$\frac{\partial(dS)}{\partial V_r} = \frac{1}{2}\rho c \cdot dr \cdot \left[\frac{\partial(V_{Rel}^2)}{\partial V_r} C_t + V_{Rel}^2 \frac{\partial C_t}{\partial V_r}\right]. \quad (A.\ 11)$$

The expression for the terms in Equations (A. 8) to (A. 11) can be expressed as follows:

$$\frac{\partial(V_{Rel}^2)}{\partial V_0} = 2V_0(1-a)^2 - V_0^2 \cdot 2(1-a)\frac{\partial a}{\partial V_0} + V_r^2 \cdot 2(1+a^{'})\frac{\partial a^{'}}{\partial V_0} \quad (A.\ 12)$$

where $\frac{\partial a}{\partial V_0} = \frac{da}{d\phi} \cdot \frac{\partial \phi}{\partial V_0}$ and $\frac{\partial a^{'}}{\partial V_0} = \frac{da^{'}}{d\phi} \cdot \frac{\partial \phi}{\partial V_0}$;

Then

$$\frac{\partial(V_{Rel}^2)}{\partial V_r} = -V_0^2 \cdot 2(1-a)\frac{\partial a}{\partial V_r} + 2V_r\left(1+a^{'}\right)^2 + V_r^2 \cdot 2(1+a^{'})\frac{\partial a^{'}}{\partial V_r} \quad (A.\ 13)$$

where $\frac{\partial a}{\partial V_r} = \frac{da}{d\phi} \cdot \frac{\partial \phi}{\partial V_r}$ and $\frac{\partial a^{'}}{\partial V_r} = \frac{da^{'}}{d\phi} \cdot \frac{\partial \phi}{\partial V_r}$.

$\frac{da}{d\phi}$ and $\frac{da^{'}}{d\phi}$ can be determined from Equations (A. 3) and (A. 4):

$$\frac{da}{d\phi} = \frac{-4\left(sin2\phi C_n - \frac{dC_n}{d\phi}sin^2\phi\right)}{\sigma C_n^2\left(\frac{4sin^2\phi}{\sigma C_n} + 1\right)^2}, \quad (A.\ 14)$$

and

$$\frac{da^{'}}{d\phi} = \frac{-4\left(cos2\phi C_t - \frac{dC_t}{d\phi}sin\phi cos\phi\right)}{\sigma C_t^2\left(\frac{4sin\phi cos\phi}{\sigma C_t} - 1\right)^2}. \quad (A.\ 15)$$

The expressions for $\frac{\partial \phi}{\partial V_0}$ and $\frac{\partial \phi}{\partial V_r}$ can be found from Equation (A. 7) using the following two equations:

$$\frac{\partial \phi}{\partial V_0}\left[\frac{d\left(\frac{1+a^{'}}{1-a}\right)}{d\phi}tan\phi+\frac{1}{cos^2\phi}\cdot\frac{1+a^{'}}{1-a}\right]=\frac{1}{V_r} \quad (A.16)$$

and

$$\frac{\partial \phi}{\partial V_r}\left[\frac{d\left(\frac{1-a}{1+a^{'}}\right)}{d\phi}cot\phi-\frac{1}{sin^2\phi}\cdot\frac{1-a}{1+a^{'}}\right]=\frac{1}{V_0}. \quad (A.17)$$

where $\frac{d\left(\frac{1+a^{'}}{1-a}\right)}{d\phi}=\frac{\frac{da^{'}}{d\phi}(1-a)+\frac{da}{d\phi}(1+a^{'})}{(1-a)^2}$ and $\frac{d\left(\frac{1-a}{1+a^{'}}\right)}{d\phi}=\frac{-\frac{da}{d\phi}(1+a^{'})-\frac{da^{'}}{d\phi}(1-a)}{(1+a^{'})^2}$.

For $\frac{\partial C_n}{\partial V_0}$, $\frac{\partial C_n}{\partial V_r}$, $\frac{\partial C_t}{\partial V_0}$ and $\frac{\partial C_t}{\partial V_r}$, the following four equations can be used:

$$\frac{\partial C_n}{\partial V_0}=\frac{dC_n}{d\phi}\cdot\frac{\partial \phi}{\partial V_0}; \quad (A.18)$$

$$\frac{\partial C_n}{\partial V_r}=\frac{dC_n}{d\phi}\cdot\frac{\partial \phi}{\partial V_r}; \quad (A.19)$$

$$\frac{\partial C_t}{\partial V_0}=\frac{dC_t}{d\phi}\cdot\frac{\partial \phi}{\partial V_0}; \quad (A.20)$$

$$\frac{\partial C_t}{\partial V_r}=\frac{dC_t}{d\phi}\cdot\frac{\partial \phi}{\partial V_r}. \quad (A.21)$$

$\frac{dC_n}{d\phi}$ and $\frac{dC_t}{d\phi}$ can be simply derived from Equations(A. 5) and (A. 6):

$$\frac{dC_n}{d\phi}=\frac{\partial C_l}{\partial \phi}cos\phi+\frac{\partial C_d}{\partial \phi}sin\phi+C_d cos\phi-C_l sin\phi, \quad (A.22)$$

and

$$\frac{dC_t}{d\phi}=\frac{\partial C_l}{\partial \phi}sin\phi-\frac{\partial C_d}{\partial \phi}cos\phi+C_l cos\phi+C_d sin\phi. \quad (A.23)$$

This provides all the terms required to determine damping derivatives.

Appendix B

Influence of non-uniform, turbulent wind field and blade flexibility

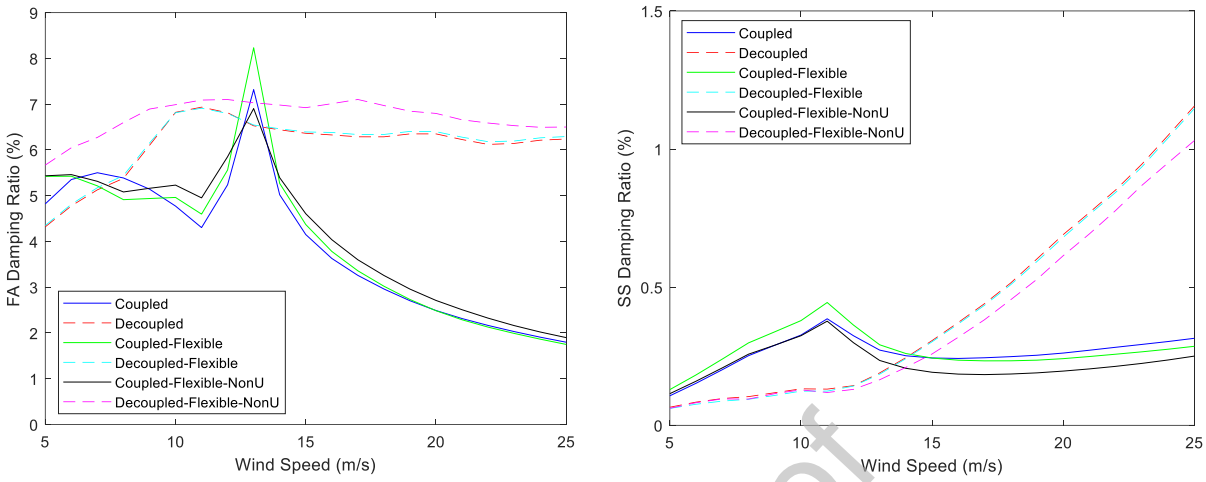

(a) (b)

Figure B.1. FA (a) and SS (b) damping ratios for the first bending modes, estimated from decay in time domain. Comparisons between the model considering only one DOF (dashed) and the coupled two DOFs model (solid) for the different models (rigid blades, uniform wind; flexible blades, uniform wind; flexible blades, turbulent wind).

Rotor blade flexibility and turbulent inflow wind fields were not considered in the proposed model to allow for simpler analytical derivation. Their influence on apparent damping was investigated using simulations including these effects in the FAST model and compared to the developed model considering only rigid blades and uniform wind fields. As shown in Figure 6 in section 4.1.2, including the blade flexibility in the FAST model for a uniform inflow wind field leads to a slight shift of about 3% of the tower resonance frequency, but only small changes in the damping visible from the time signal decay. Using the same methodology as in Section 4.4.2, the influence on the damping ratios was quantified and is shown in Figure B.1. For the decoupled systems, almost no discernible difference was found in either direction, as the system responds with an exponential decay (as expected from a single degree of freedom system) and the change in resonance frequency does not lead to a change in the decay envelope. For the coupled system, some differences in the estimated damping ratios are visible in the FA direction below the rated wind speed (Figure B.1 (a)), where consideration of the blade flexibility leads to approximately constant damping values up to 12 m/s wind speed. For higher wind speeds in the FA direction, the general dependence of the

damping ratios follows a similar trend, but with differences of up to 0.21% damping ratio. In the SS direction, the damping ratios follow a similar pattern, but again differences of up to 0.06% damping ratio were found due to the inclusion of the realistic blade flexibility.

Quantification of the damping ratios for non-uniform inflow wind fields in the time domain is more complex, as the turbulence leads to a continuous energy input and thus excitation of tower vibrations. Simulations were run in FAST for an initial 1m displacement and for the same conditions without the initial displacement. Subtracting the respective responses to eliminate the turbulence excitation, the damping ratios were quantified as described in section 4.4.2 and averaged over 10 different seeds for the turbulent wind field for each case. For the decoupled system, the consideration of turbulence leads to a similar behaviour of damping ratios on wind speed, but consistently higher damping ratios of up to 1.35% in the FA direction and lower values of up to 0.12% in the SS direction, due to the interaction of the flexible blades with the turbulent wind field. For the coupled system, again the dependence of damping ratios for all three cases follows a similar trend, with differences of up to 0.86% in the FA direction and 0.06% in the SS direction. This is in line with the results of Valamanesh and Myers [11], who found that the assumption of rigid blades leads to variations of damping estimates by approximately 1%. Therefore, we conclude that the main influence on the damping considering coupled or decoupled tower vibrations for an operating wind turbine can be reasonably well captured by the aerodynamic damping matrix derived assuming rigid blades. However, the influence of blade flexibility and turbulent wind fields on the overall tower damping should be considered for detailed predictions including the coupling between FA and SS directions, as it can change the apparent damping ratios by up to 0.86%.

Author statement

Chao Chen: Conceptualization, Formal analysis, Methodology, Software, Validation, Writing - Original Draft

Philippe Duffour: Conceptualization, Supervision, Writing - Review & Editing

Paul Fromme: Supervision, Methodology, Writing - Review & Editing

Declaration of interests

☒ The authors declare that they have no known competing financial interests or personal relationships that could have appeared to influence the work reported in this paper.

References

[1] Jonkman JM, Buhl MLJ. *FAST user's guide*. Technical Report NREL/EL-500-38230. National Renewable Energy Laboratory: Golden, CO, USA, October 2005.

[2] Torben J, Melchior A, Version D. *How 2 HAWC2, the user's manual*. Technical Report Risø-R-1597(ver. 3-1)(EN). Risø National Laboratory, Denmark, 2007.

[3] Hansen M. *Aerodynamics of wind turbines*. Second Edi. Routledge, 2008.

[4] Rezaei R, Fromme P, Duffour P. Fatigue life sensitivity of monopile-supported offshore wind turbines to damping. *Renew Energy* 2018; 123: 450–459.

[5] Muskulus M, Schafhirt S. Reliability-based design of wind turbine support structures. In: *Proceedings of the Symposium on Reliability of Engineering System*. Hangzhou, China, 2015.

[6] Bisoi S, Haldar S. Dynamic analysis of offshore wind turbine in clay considering soil–monopile–tower interaction. *Soil Dyn Earthq Eng* 2014; 63: 19–35.

[7] Muskulus M. Simplified rotor load models and fatigue damage estimates for offshore wind turbines. *Philos Trans R Soc London A Math Phys Eng Sci* 2015; 373: 20140347.

[8] Schafhirt S, Muskulus M. Decoupled simulations of offshore wind turbines with reduced rotor loads and aerodynamic damping. *Wind Energy Sci* 2018; 3: 25.

[9] Shirzadeh R, Devriendt C, Bidakhvidi MA, et al. Experimental and computational damping estimation of an offshore wind turbine on a monopile foundation. *J Wind Eng Ind Aerodyn* 2013; 120: 96–106.

[10] Rezaei R, Duffour P, Fromme P. Scour influence on the fatigue life of operational monopile-supported offshore wind turbines. *Wind Energy* 2018; 1–14.

[11] Valamanesh V, Myers AT. Aerodynamic damping and seismic response of horizontal axis wind turbine towers. *J Struct Eng* 2014; 140: 1–9.

[12] Salzmann DJC, Tempel J Van Der. Aerodynamic damping in the design of

support structures for offshore wind turbines. In: *The European Offshore Wind Conference & Exhibition*. Copenhagen, Denmark, 2005.

[13] Ozbek M, J. Rixen D. Operational modal analysis of a 2.5 MW wind turbine using optical measurement techniques and strain gauges. *Wind Energy* 2013; 17: 367–381.

[14] Tarp-Johansen NJ, Andersen L, Christensen ED, et al. Comparing sources of damping of cross-wind motion. In: *Proceeding of the Copenhagen Offshore Conference*. Stockholm, Sweden, 2009.

[15] Devriendt C, Weijtjens W. *Damping of offshore wind turbines*. Poster presented in Offshore Wind Energy 2017, London 6-8 June, 2017.

[16] Hansen MH, Thomsen K, Fuglsang P, et al. Two methods for estimating aeroelastic damping of operational wind turbine modes from experiments. *Wind Energy* 2006; 9: 179–191.

[17] Koukoura C, Natarajan A, Vesth A. Identification of support structure damping of a full scale offshore wind turbine in normal operation. *Renew Energy* 2015; 81: 882–895.

[18] Weijtjens W, Rasoul Shirzadeh, Gert De Sitter, et al. Classifying resonant frequencies and damping values of an offshore wind turbine on a monopile foundation for different operational conditions. In: *Proceedings of the European Wind Energy Association*. Barcelona, Spain, 2014.

[19] Hu W-H, Thöns S, Rohrmann RG, et al. Vibration-based structural health monitoring of a wind turbine system. Part I: Resonance phenomenon. *Eng Struct* 2015; 89: 260–272.

[20] Dong X, Lian J, Wang H, et al. Structural vibration monitoring and operational modal analysis of offshore wind turbine structure. *Ocean Eng* 2018; 150: 280–297.

[21] Dai K, Wang Y, Huang Y, et al. Development of a modified stochastic subspace identification method for rapid structural assessment of in-service utility-scale wind turbine towers. *Wind Energy* 2017; 17: 657–669.

[22] Chen C, Duffour P. Modelling damping sources in monopile-supported offshore wind turbines. *Wind Energy* 2018; 21: 1121–1140.

[23] Freris LL. *Wind energy conversion systems*. New York: Prentice Hall, 1990.

[24] Kühn M. *Dynamics and design optimization of offshore wind energy conversion systems*. PhD Thesis. Delft University of Technology, 2001.

[25] Chen B, Zhang Z, Hua X, et al. Identification of aerodynamic damping in wind turbines using time-frequency analysis. *Mech Syst Signal Process* 2017; 91: 198–214.

[26] Liu X, Lu C, Li G, et al. Effects of aerodynamic damping on the tower load of offshore horizontal axis wind turbines. *Appl Energy* 2017; 204: 1101–1114.

[27] Petersen JT, Madsen H a, Bjorck A, et al. *Prediction of dynamic loads and induced vibrations in stall*. Technical Report NO. 1045(EN). Forskningscenter Risoe, Denmark, 1998.

[28] Jonkman JM, Butterfield S, Musial W, et al. *Definition of a 5-MW reference wind turbine for offshore system development*. Technical Report NREL/TP-500-38060. National Renewable Energy Laboratory: Golden, CO, USA, 2009.

[29] Tempel J Van Der. *Design of support structures for offshore wind turbines*. PhD Thesis. Delft University of Technology, 2006.

[30] Belytschko T, Hughes TJ. *Computational methods for transient analysis*. Amsterdam: North-Holland, 1983.

[31] Gutiérrez-Wing ES. *Modal analysis of rotating machinery structures*. PhD Thesis. Imperial College London, 2003.

[32] Devriendt C, Magalhaes F, Weijtjens W, et al. Structural health monitoring of offshore wind turbines using automated operational modal analysis. *Struct Heal Monit* 2014; 13: 644–659.

[33] Bajrić A, Høgsberg J, Rüdinger F. Evaluation of damping estimates by automated Operational Modal Analysis for offshore wind turbine tower vibrations. *Renew Energy* 2018; 116: 153–163.

[34] Jonkman JM, Hayman GJ, Jonkman BJ, et al. *AeroDyn v15 user's guide and theory manual*. Technical Report. National Renewable Energy Laboratory: Golden, CO, USA, 2015.

[35] Devriendt C, Jordaens PJ, De Sitter G, et al. Damping estimation of an offshore wind turbine on a monopile foundation. In: *EWEA 2012*. Copenhagen, Denmark, 2012.

[36] Adhikari S, Woodhouse J. Identification of damping: Part 1, viscous damping. *J Sound Vib* 2001; 243: 43–61.

[37] Hodges CH, Power J, Woodhouse J. The use of the sonogram in structural acoustics and an application to the vibrations of cylindrical shells. *J Sound Vib* 1985; 101: 203–218.

[38] Ozbek M, Meng F, Rixen DJ. Challenges in testing and monitoring the in-operation vibration characteristics of wind turbines. *Mech Syst Signal Process* 2013; 41: 649–666.

[39] Fontecha R, Kemper F, Feldmann M. On the Determination of the Aerodynamic Damping of Wind Turbines Using the Forced Oscillations Method in Wind Tunnel Experiments. *Energies* 2019; 12: 2452.